Tailoring the interfacial active center of MnS$_x$O$_{2-x}$/MnCo$_2$S$_4$ heterostructure to boost the performance for oxygen evolution reaction and Zn-Air batteries in neutral electrolyte

Kai Wang [a,1], Zheng Wang [b,1], Yonggang Liu [a], Jiapeng Liu [b], Zhiming Cui [c], Xiaofeng Zhang [d], Francesco Ciucci [b,e], Zhenghua Tang [a,c,*]

[a] *Guangzhou Key Laboratory for Surface Chemistry of Energy Materials and New Energy Research Institute, School of Environment and Energy, South China University of Technology, Guangzhou Higher Education Mega Centre, Guangzhou 510006, China*

[b] *Department of Mechanical and Aerospace Engineering, The Hong Kong University of Science and Technology, Hong Kong, 999077, SAR, China*

[c] *Key Laboratory of Fuel Cell Technology of Guangdong Province, School of Chemistry and Chemical Engineering, South China University of Technology, Guangzhou 510640, China*

[d] *Institute of New Materials, Guangdong Academy of Science, Guangzhou 510650, China*

[e] *Department of Chemical and Biological Engineering, The Hong Kong University of Science and Technology, Hong Kong 999077, SAR, China*
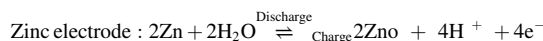
ARTICLE INFO

ABSTRACT

Tailoring interfaces in heterostructured electrocatalysts is an optimal strategy for improving the electrocatalytic performance, yet determining which active center to adjust is still extremely challenging. Herein, we report a facile approach to construct a novel heterostructured electrocatalyst of MnS$_x$O$_{2-x}$/MnCo$_2$S$_4$. The density and structure of the active centers were fine-tuned by controlling the S-O atomic ratio on the surface of MnS$_x$O$_{2-x}$. Consequently, the optimized MnS$_{0.10}$O$_{1.90}$/MnCo$_2$S$_4$ sample had excellent oxygen evolution reaction performance, with overpotential of 367 mV @ 50 mA cm^{-2} in 1.0 M KOH. More impressively, in 0.2 M phosphate buffer solution, the overpotential @ 10 mA cm^{-2} is only 414 mV. Furthermore, as the air–cathode catalyst in neutral zinc-air batteries, MnS$_{0.10}$O$_{1.90}$/MnCo$_2$S$_4$ exhibited excellent stability with the round-trip efficiency decaying by only 3.8% at 10 mA cm^{-2} after 140 h. Theoretical calculations revealed that Mn-Co site has the suitable binding affinity to the oxygen-containing intermediates, neither too weak (Mn site) nor too strong (Co-Co site), while MnCo$_2$S$_4$ endows the oxidized CoMnO active species a tensile strain that decreases the overpotential. This study opens an avenue for developing high-performance and durable heterostructure electrocatalysts toward OER, metal-air batteries in neural electrolytes and beyond.

1. Introduction

Oxygen evolution reaction (OER) is the primary half-cell reaction that occurs at the cathode for several electrochemical energy storage and conversion devices, such as rechargeable metal-air batteries, water splitting, and photoelectrochemical cells [1–4]. Zinc-air batteries (ZABs) are one of the most promising clean energy devices for realizing the next generation green energy demand due to their low cost, high safety, and large theoretical energy density [5–7]. To improve ionic conductivity, oxygen diffusivity rate, and electrode activity, ZABs usually operate in alkaline electrolytes such as KOH and NaOH [8–10]. However, when the ZABs operate continuously for prolonged duration, such electrolyte can
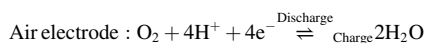
absorb CO$_2$ from the environment and form carbonates, significantly blocking the air diffusion layer hence greatly shortening the lifetime of ZABs. Neutral electrolytes are environmentally friendly and safe, overcoming the limitations of highly concentrated alkaline electrolytes including corrosion, carbonation, and zinc dendrite growth [11,12]. ZnCl$_2$-NH$_4$Cl buffer is a commonly used neutral electrolyte for ZABs, in which the electrochemical reactions are the same as in acid conditions. The half-cell reactions are described as follows [13,14]:

$$\text{Zinc electrode}: 2\text{Zn} + 2\text{H}_2\text{O} \underset{\text{Charge}}{\overset{\text{Discharge}}{\rightleftharpoons}} 2\text{Zno} + 4\text{H}^+ + 4\text{e}^-$$

Air electrode : $O_2 + 4H^+ + 4e^- \underset{\text{Charge}}{\overset{\text{Discharge}}{\rightleftharpoons}} 2H_2O$

Despite the great promise of neutral ZABs, there are still some key issues that limit their further large-scale commercialization. One critical problem is that, the H^+ concentration is quite low in neutral media, thus high overpotentials are needed to evolve oxygen. Therefore, it is imperative to develop highly active and durable OER catalysts in neutral electrolyte [15–17]. Currently, noble metal oxides such as IrO_2 and RuO_2 are considered as state-of-the-art OER catalysts. However, the high cost and low natural abundance of Ir and Ru have significantly restricted their commercialization in ZABs.

In light of the need for non-precious-metal-based OER catalysts with cost-effectiveness, high efficiency, and robust durability, transition-metal-based catalysts including transition metal oxides [18–21], hydroxides [22–24], and chalcogenides [25,26], have aroused enormous interests as alternatives. Among them, transition metal-sulfides (TMSs) have been attracting tremendous attentions due to their high conductivity, facile synthesis, and excellent activity [27,28]. Fine-tuning the composition and structure of TMSs has been proved to be effective in optimizing their electrocatalytic performance [24,29]. Among various TMSs materials, heterostructured TMSs are widely recognized as one of the most promising non-noble-metal based OER catalysts owing to their high density of active sites (such as edges, corners, defects, and vacancies) at the interface [30,31]. For instance, Zhang et al. developed a tremella-like Ni_3S_2/MnS material with ultrathin nanosheets and rich oxygen vacancies on nick foam [25], and importantly, the material exhibited superior OER activity because of the high density of oxygen vacancies at the Ni_3S_2/MnS interface. In another study, the Feng group verified that the interfacial synergism of MoS_2/Ni_3S_2 is beneficial to the chemisorption of oxygen-containing intermediates, which accelerates the occurrence of the OER process [32]. Apart from the above work, a manifold of theoretical simulations and experimental results have revealed that, the properties of the heterostructure catalysts can be governed by their interfacial structure [33,34]. However, it is still extremely challenging to manipulate the heterostructure interfacial properties such as charge transfer, tensile strain, and active site to lower the overpotential so as to boost the OER performance.

Herein, we present a facile strategy to regulate the interfacial and electronic structure in the novel MnS_xO_{2-x}/$MnCo_2S_4$ heterostructure. In the obtained MnS_xO_{2-x}/$MnCo_2S_4$ heterostructure, the outer $MnCo_2S_4$ nanoparticles are anchored on the surface of the internal MnS_xO_{2-x} nanorods, resulting in abundant interfaces. In addition, the electronic and lattice structure of the heterogeneous interface can be easily optimized by controlling the vulcanized conditions to adjust the sulfur-to-oxygen ratio. The experimental results reveal that the sulfur-to-oxygen ratio of MnS_xO_{2-x} nanorods plays a crucial role in regulating the electronic and lattice structure of the MnS_xO_{2-x}/$MnCo_2S_4$ interface. Specifically, $MnS_{0.1}O_{1.9}$/$MnCo_2S_4$ (x = 0.1) maintains an intact nanorod-like structure with a high-density of heterogeneous interface. Formation of oxygen vacancies can be promoted by regulating the ratio of S-to-O, *i.e.*, x. The $MnS_{0.10}O_{1.90}$/$MnCo_2S_4$ catalyst exhibits outstanding activity and durability for OER in neutral and alkaline electrolyte, superior to the commercial IrO_2 catalyst. Density functional theory (DFT) calculations revealed that the strong interfacial interactions between MnS_xO_{2-x} and $MnCo_2S_4$ in the MnS_xO_{2-x}/$MnCo_2S_4$ heterostructure is crucial to its high electrocatalytic performance. On one hand, the electron flow occurring at the interface from $MnCo_2S_4$ to MnO_2 significantly increases the conductivity of the catalyst. On the other hand, due to the tensile strain of the CoMnO-S interfacuak moieties, the energy difference between O* and OOH* intermediates can be reduced hence drastically decreasing the OER overpotential.

2. Experimental section

2.1. Materials

Potassium permanganate ($KMnO_4$) and ammonium chloride (NH_4Cl) were purchased from Guangzhou Chemical Reagent Factory (Guangzhou, China), cobalt (II) acetate tetrahydrate ($Co(OAc)_2 \cdot 4H_2O$), manganese(II) acetate tetrahydrate ($Mn(OAc)_2 \cdot 4H_2O$), thioacetamide (TAA), potassium hydroxide (95% KOH) and ethanol were obtained from Energy Chemicals (Shanghai, China). Nafion (5 wt%) was acquired from Dupont (USA). All aqueous solutions were prepared using deionized (DI) water with a resistivity of 18.3 MΩ·cm.

2.2. Preparation of MnO_2 nanorods

MnO_2 nanorods were prepared by following the typical hydrothermal method. Specifically, 0.625 mmol $KMnO_4$ and 0.625 mmol NH_4Cl were added into 50 mL deionized H_2O, and the mixture was kept stirring for 5 min at room temperature. Subsequently, the solution was transferred into a 100 mL Teflon-lined autoclave and maintained in an oven at 140 °C for 24 h. Finally, it was washed with deionized water and ethanol several times and then dried at 40 °C for 12 h in a vacuum oven.

2.3. Preparation of MnS_xO_{2-x}/$MnCo_2S_4$ heterostructure nanorods

Firstly, 0.2 mmol $Mn(OAc)_2 \cdot 4H_2O$ and 0.4 mmol $Co(OAc)_2 \cdot 4H_2O$ were dissolved into 100 mL ethanol, and 50 mg of the above obtained MnO_2 sample was added into the solution. After ultrasonic treatment for 30 mins, the suspension was transferred to the oil bath and kept stirring at 80 °C for 4 h, then the product was rinsed by ethanol for 3 times, and the obtained sample was denoted by MnO_2/$(MnCo)_5(OH)_2(OAc)_8$ (marked as MnO_2/MCOA). Subsequently, the above sample and TAA (0.2, 0.4, 0.6, and 0.8 mmol) were added into 40 mL ethanol, and the solution was kept stirring for 5 min at room temperature. Finally, the mixture was transferred into the 100 mL Teflon-lined autoclave and kept in the oven under 120 °C for 12 h, washed with ethanol 3 times and dried at 40 °C for 12 h in a vacuum oven, and the collected solid is the final product denoted as MnS_xO_{2-x}/$MnCo_2S_4$ (x represents the S stoichiometric ratio in MnO_2). The MnS_xO_{2-x}/$MnCo_2S_4$ formed by vulcanization of different molar amounts of TAA was also marked as S-0.2, S-0.4, S-0.6, and S-0.8, respectively.

2.4. Electrochemical measurements

The electrochemical tests were performed on the CHI 750E electrochemical workstation (CH Instruments, Chenhua Co Ltd., China) using a three-electrode cell (Hg/HgO as the reference electrode, carbon rod as the counter electrode) at room temperature. The catalyst modified glassy carbon rotating ring-disk electrode (RRDE, Pine instrument company, LLC) with diameter of 5 mm was employed as the working electrode. The catalyst ink was prepared as follows: 2 mg of the as-prepared catalyst was dispersed ultrasonically in 0.4 mL nafion/ethanol (1.0% nafion) to form a homogeneous suspension with a concentration of was 5 mg mL^{-1}. 10 μL suspension was then dropcast onto the surface of the polished glassy carbon electrode, dried at room temperature. The loading amount of the catalyst was calculated to be 255.1 μg cm^{-2}. The electrochemically active surface areas (ECSAs) of the catalysts were calculated from electrochemical double-layer capacitance (C_{dl}) of the sample. ECSA = R_f/S, in which S stands for the real surface area of the smooth metal electrode, which is generally equaling to the geometric area of working electrode (in this work, S = 0.196 cm^2). The roughness factor R_f was estimated from the ratio of double-layer capacitance C_{dl} for the working electrode and the corresponding smooth metal electrode (assuming that the average double-layer capacitance of a smooth metal oxide surface is 60 μF cm^{-2}), that is, R_f = C_{dl}/60 μF cm^{-2} [35]. The C_{dl} value was determined via cyclic

voltammograms with a potential region where no obvious Faradaic process occurs. The double-layer charging current I_c can be related to the scan rates (v) through Equation 1: $I_c = C_{dl} \times v$. Therefore, the charging current at a specific potential has a linear relationship with the scanning rates, and its slope is the C_{dl} value. Linear sweep voltammograms (LSVs) were obtained at a sweep rate of 10 mV s^{-1} in N$_2$ -saturated 1 M KOH or 0.2 M PBS solution at various rotation rates 1600 rpm. The electrochemical impedance spectroscopic (EIS) spectrum was recorded in the frequency range from 100 kHz to 0.01 Hz employing A.C. impedance technique with the amplitude of 0.005 V. The long-term stability test was performed using amperometric i-t measurement at 1.6 V ($vs.$ RHE) in 0.2 M PBS solution. The Hg/HgO electrode was calibrated with a reversible hydrogen electrode (RHE), $E_{RHE} = E_{Hg/HgO} + 0.098$ (V) + 0.0591*(pH).

2.5. Battery test

The Zn-air battery was self-assembled by using the zinc plate as the anode, the catalyst loaded on carbon cloth as the air–cathode, and 5 M NH$_4$Cl plus 0.25 M ZnCl$_2$ as the electrolyte. The air–cathode was fabricated by the following process: 2 mg catalyst was dispersed into 400 μL Nafion/ethanol solution (0.5%), and then subject to ultrasonic treatment for ~30 mins. Subsequently, the prepared suspension was dropcast onto the hydrophobic side of the carbon cloth and ensuring the effective area was 1 cm^2. All zinc-air battery tests were carried out by the CHI-440 electrochemical workstation (CH Instruments, Chenhua Co Ltd., China) and LAND CT2001A battery program-control test system at ambient conditions. The characterization, and simulation methods can be found in Supplementary materials.

3. Results and discussions

The route for synthesizing the MnS$_x$O$_{2-x}$/MnCo$_2$S$_4$ heterostructure are shown in Scheme 1 (Supplementary Material). Firstly, the one-dimensional (1 D) MnO$_2$ nanorods were synthesized by a simple hydrothermal reaction. Specifically, KMnO$_4$ was reduced into MnO$_2$ by NH$_4$Cl, while NH$_4$Cl was oxidized into N$_2$, thus increasing the pressure of the reaction system, which triggered the formation of uniform MnO$_2$ nanorods. A probable mechanism is proposed as follows: Firstly, under hydrothermal conditions, the MnO$_x$ units appear first in the solution, and then through a condensation reaction, they form MnO$_2$ sheets. Subsequently, the layer structure of MnO$_2$ tends to curl at an elevated temperature and pressure, and this is the critical step for the formation of one-dimensional MnO$_2$ nanostructure. Finally, the tubular structure is formed in the reaction system [36]. Subsequently, the MnO$_2$ nanorods were used as the skeleton for the growth of (MnCo)$_5$(OH)$_2$(OAc)$_8$ (MCOA) through a coprecipitation process. Finally, using TAA as the sulfur source, the above as-prepared MnO$_2$/MCOA composite was

vulcanized to form MnS$_x$O$_{2-x}$/MnCo$_2$S$_4$ nanorods. During this process, MCOA was completely vulcanized into MnCo$_2$S$_4$, while only part of the O^{2-} anions in MnO$_2$ exchanged with S^{2-} to form MnS$_x$O$_{2-x}$.

The fabrication process was characterized by electronic microscopic technique. As shown in Fig. 1a, the as-prepared MnO$_2$ exhibits an ultralong nanorod morphology with a diameter of 47.9 ± 3.1 nm. After depositing MCOA, the MnO$_2$/MCOA inherits the fine nanorod morphology of MnO$_2$, as presented in Fig. S1a. However, the diameter of MnO$_2$/MCOA increased to 60.3 ± 2.4 nm. Subsequently, we explored the effect of the TAA amount on the structure of MnS$_x$O$_{2-x}$/MnCo$_2$S$_4$. When the amount of TAA is 0.2 mmol, only a few nanoparticles appear on the nanorods' surface (Fig. S1b). Interestingly, if TAA is increased to 0.4 mmol, particles are densely and uniformly distributed on the nanorods (Fig. 1b). When further increasing the molar quantity of TAA to 0.6 mmol, part of the nanorods were converted into nanoparticles (Fig. S1c), and when the TAA amount reaches 0.8 mmol, the nanorods structure disappeared, as depicted in Fig. S1d. The above results indicate that, the S-0.4 (0.4 mmol TAA) sample possesses the optimal well-defined heterostructure, hence it was chosen for further characterizations.

To observe the surface microstructure, transmission electron microscopy (TEM) and high-resolution TEM (HR-TEM) were then carried out on the S-0.4 sample (MnS$_{0.10}$O$_{1.90}$/MnCo$_2$S$_4$). As illustrated in Fig. 1c and d, plentiful nanoparticles are anchored onto the nanorods, and the average diameter of the nanoparticles is 11.5 ± 3.2 nm. Furthermore, the crystal structure of MnO$_2$ and the S-0.4 sample was examined by X-ray diffraction (XRD). As shown in Fig. 2a, the diffraction peaks of $2\theta = 12.69°$, 18.00°, 25.02°, 28.70°, 36.64°, 37.49°, and 65.83° can be assigned to the (110), (200), (220), (310), (400), (211), and (112) crystal planes of the α-phase MnO$_2$ (JCPDS No. 44-0141) [37,38], respectively. It can be noted that, after vulcanization, the (110) and (220) peaks from MnO$_2$ are much weaker and almost disappear, while the (200) peaks are more pronounced, suggesting that the lattice structure of MnO$_2$ is defective owing to part of the O^{2-} anions are replaced by S^{2-} [39]. Meanwhile, the new diffraction peaks appear at 30.68°, 32.60°, and 38.40°, which can be ascribed to (311), (222), and (400) lattice planes of MnCo$_2$S$_4$ (JCPDS No. 73-1703) [40], respectively. In addition, as shown in Fig. S2, there are both Mn$_2$O$_3$ and MnS lattices in MnS$_x$O$_{2-x}$, indicating that MnO$_2$ is partially reduced during the sulfidation process.

The HR-TEM (Fig. 1e) image suggests that there are two kinds of adjacent lattice fringes with the interplanar spacings of ~0.28 nm and ~0.48 nm in the S-0.4 sample, which belong to the (311) and (200) crystal plane of MnCo$_2$S$_4$ and MnO$_2$, respectively. Moreover, a plethora of lattice defects exist at the MnS$_{0.10}$O$_{1.90}$/MnCo$_2$S$_4$ heterostructure interfaces, and some are marked in the white circles in Fig. 1e. The high-angle annular dark-field scanning TEM (HAADF-STEM) and corresponding mapping images (Fig. 1f) strongly substantiate that Mn, Co, S, and O elements are all present throughout the MnS$_{0.10}$O$_{1.90}$/MnCo$_2$S$_4$ heterostructure nanorods. In addition, the line scanning profile (Fig. 1g) indicates that the Mn and O elements are mainly distributed on the nanorods, while the concentrations of S and Co elements are higher on the outer nanoparticles. These results imply that MnCo$_2$S$_4$ nanoparticles are anchored onto the MnS$_{0.10}$O$_{1.90}$ nanorods surface to form the heterostructure, which are consistent with the XRD observations, further verifying the formation of the MnS$_x$O$_{2-x}$/MnCo$_2$S$_4$ heterostructure, and abundant lattice defects exist in the S-0.4 sample.

Subsequently, the composition and charge state of the MnS$_x$O$_{2-x}$/MnCo$_2$S$_4$ series (S-0.2, S-0.4, S-0.6, and S-0.8) and the MnO$_2$/MCOA sample were analyzed by X-ray photoelectron spectroscopy (XPS). As shown in Fig. S3, the Co, Mn, and O elements are present in all samples, while S only exists in the S-0.2, S-0.4, S-0.6, and S-0.8 samples, confirming that the samples were successfully sulfurized. Furthermore, the percentage of each element in all catalysts detected by XPS is summarized in Table S1, and the values of x in all vulcanized samples are calculated using Eq. (2):
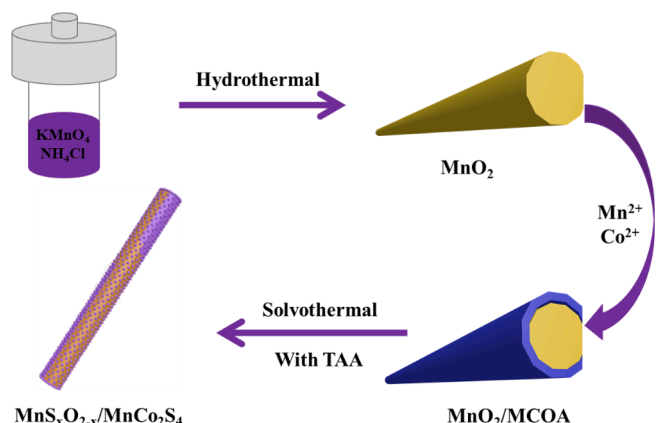
Scheme 1. Illustration for fabrication of the MnS$_x$O$_{2-x}$/MnCo$_2$S$_4$ catalyst.
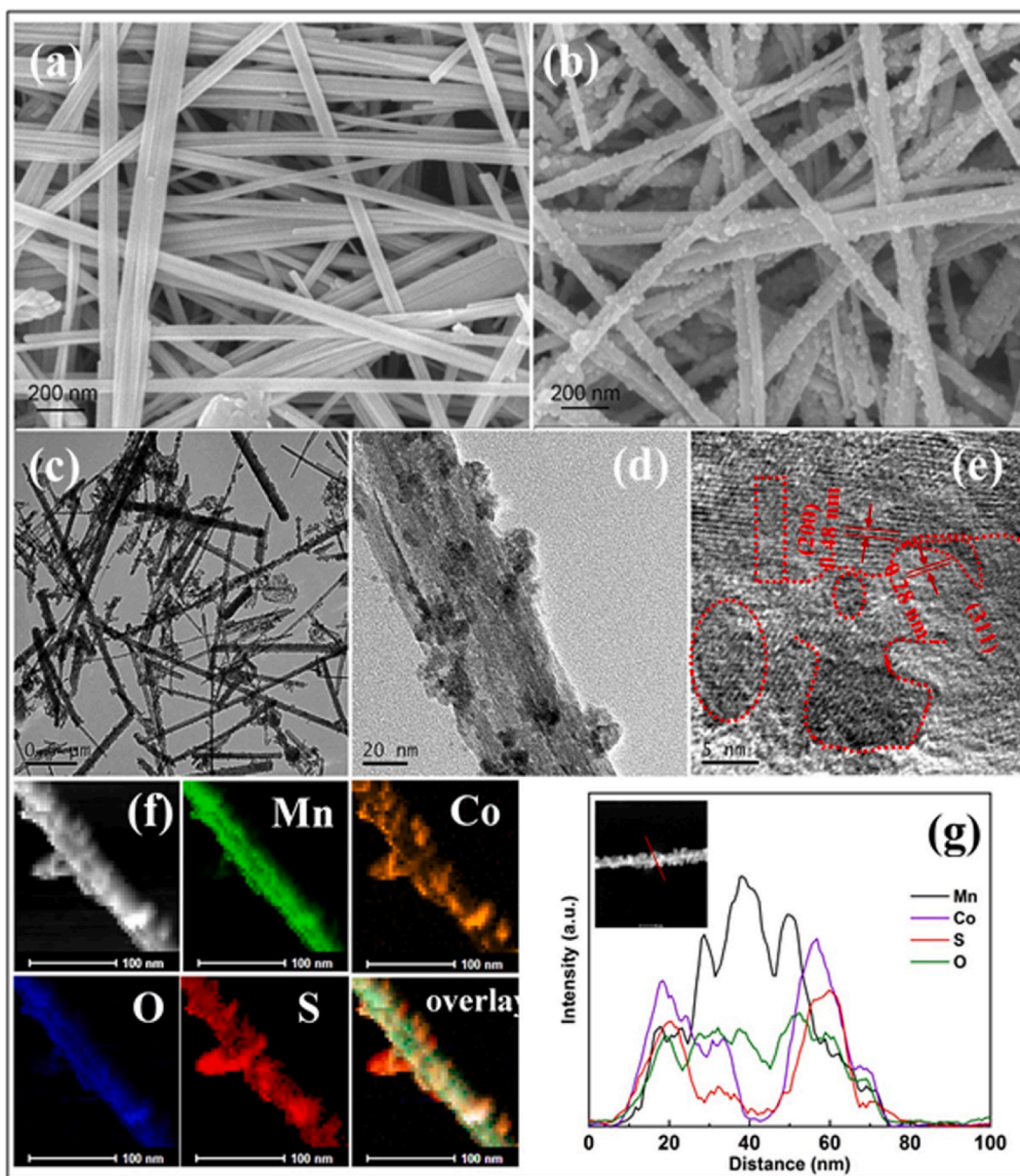
Fig. 1. (a) and (b) SEM images of MnO_2 and $MnS_{0.10}O_{1.90}/MnCo_2S_4$. (c) and (d) TEM micrographs of $MnS_{0.10}O_{1.90}/MnCo_2S_4$. (e) HR-TEM image of $MnS_{0.10}O_{1.90}/MnCo_2S_4$. (f) HAADF-STEM images and corresponding EDX elemental maps of $MnS_{0.10}O_{1.90}/MnCo_2S_4$, and (g) Line-scanning profiles of Mn, Co, O, and S along the red line in the inset.

$$x = \frac{S_{total\ atomic\ percent} - 2Co_{total\ atomic\ percent}}{Mn_{total\ atomic\ percent} - \frac{1}{2}Co_{total\ atomic\ percent}} \qquad (2)$$

According to the XPS survey-scan results and Equation (2), the value of x was calculated to be 0.02, 0.10, 0.34, and 0.65, for the S-0.2, S-0.4, S-0.6, and S-0.8 sample, respectively, therefore, the corresponding molecular formulas of $MnS_xO_{2-x}/MnCo_2S_4$ can be denoted as $MnS_{0.02}O_{1.98}/MnCo_2S_4$, $MnS_{0.10}O_{1.90}/MnCo_2S_4$, $MnS_{0.34}O_{1.66}/MnCo_2S_4$, and $MnS_{0.65}O_{1.35}/MnCo_2S_4$, respectively. To investigate the effect of the initial sulfur loading on the electronic interaction between MnS_xO_{2-x} and $MnCo_2S_4$ in the $MnS_xO_{2-x}/MnCo_2S_4$ series, high-resolution XPS spectra of Mn, Co, O, and S elements were recorded. As shown in Fig. S4a, the binding energy of the Mn $2p_{3/2}$ electrons varies with the sulfur content. Compared with S-0.2, the binding energy of the Mn $2p_{3/2}$ electrons for S-0.4 and S-0.6 shifted negatively about 0.43 eV and 0.38 eV, respectively, while S-0.8 remains almost unchanged. Fig. S4b shows that the binding energies of the Co $2p_{3/2}$ electrons for the S-0.4, S-0.6, and S-0.8 samples shifted positively by 0.65 eV, 0.48 eV,

and 0.17 eV compared with that of S-0.2, respectively. It can be noted that, the S-0.4 sample ($MnS_{0.10}O_{1.90}/MnCo_2S_4$) with well-defined heterostructure has the largest binding energy shift for both Mn and Co elements. Such phenomenon can also be observed in the O 1s and S 2p XPS spectra, as presented in Fig. S5a and S5b. It demonstrates that the electronic structure of each element in $MnS_xO_{2-x}/MnCo_2S_4$ can be regulated by adjusting the sulfur content. Such XPS findings clearly demonstrate that more heterointerfaces of $MnS_xO_{2-x}/MnCo_2S_4$ can result in greater electronic structural change [34,41–43].

Subsequently, the high-resolution XPS spectra of the $MnS_{0.10}O_{1.90}/MnCo_2S_4$ sample were recorded to probe the valence state, as compared with the $MnO_2/MCOA$ sample. In the O 1s spectra (Fig. 2b) of $MnS_{0.10}O_{1.90}/MnCo_2S_4$ and $MnO_2/MCOA$, there are clearly O1, O2, and O3 three species with binding energy located at 529.9, 531.4, and 532.3 eV, corresponding to lattice oxygen, defective oxygen, and the OH^- groups adsorbed on the surface, respectively [41]. It can be noted that, $MnO_2/MCOA$ has much more O3 species, indicating plentiful water
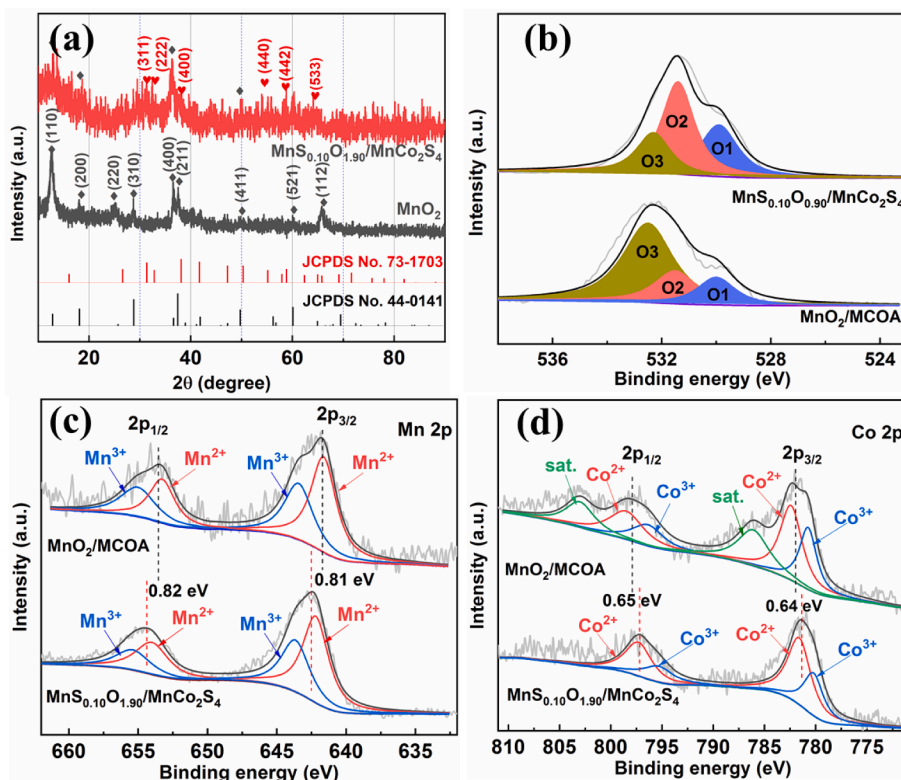
Fig. 2. (a) XRD patterns of MnO_2 and $MnS_{0.10}O_{1.90}/MnCo_2S_4$. (b), (c) and (d) are the high-resolution XPS spectra of the O 1s, Mn 2p, and Co 2p electrons from the $MnS_{0.10}O_{1.90}/MnCo_2S_4$ and $MnO_2/MCOA$ samples.

molecules are adsorbed onto the surface, forming a large number of OH^- groups. More noteworthily, $MnS_{0.10}O_{1.90}/MnCo_2S_4$ has much higher content of O2 species, suggesting that the heterostructure is formed accompanying with abundant defects. Furthermore, the electron spin resonance (ESR) spectra were acquired to confirm the vacancies. As shown in Fig. S6, the samples of S-0.4 ($MnS_{0.10}O_{1.90}/MnCo_2S_4$) and S-0.6 display obvious central symmetrical signal at ~324 mT, indicating there are abundant oxygen vacancies in both samples. It should be noted that, S-0.4 exhibits the significantly increased ESR intensity compared to S-0.6, demonstrating more oxygen vacancies were formed on the surface of S-0.4. However, the MnO_2 and S-0.2 samples show a negligible ESR signal, indicating the absence of oxygen vacancy. The high-resolution XPS spectra of Mn 2p (Fig. 2c) show that the binding energies of the Mn $2p_{3/2}$ and Mn $2p_{1/2}$ electrons in $MnS_{0.10}O_{1.90}/MnCo_2S_4$ have a positive shift of 0.81 eV and 0.82 eV compared to $MnO_2/MCOA$, respectively. Additionally, the peaks of Co $2p_{3/2}$ and Co $2p_{1/2}$ in $MnS_{0.10}O_{1.90}/MnCo_2S_4$ shift negatively of 0.64 and 0.65 eV, compared with that of $MnO_2/MCOA$ (Fig. 2d). The above results indicate that there is strong electronic interaction between $MnS_{0.10}O_{1.90}$ and $MnCo_2S_4$, which might be beneficial to the charge transfer process for OER.

The electrocatalytic OER performance of all the samples was then examined by the linear sweep voltammetry (LSV) in 1 M KOH electrolyte at first. As shown in Fig. S7a, with the increase of the vulcanization degree, the OER performance increased first then attenuated. $MnS_{0.10}O_{1.90}/MnCo_2S_4$ exhibits the most outstanding OER performance with the overpotential of 367 mV at 50 mA cm^{-2}, which is much lower than those of MnO_2 (550 mV), $MnCo_2S_4$ (423 mV), S-0.2 (405 mV), S-0.6 (420 mV), and S-0.8 (450 mV). Moreover, the corresponding Tafel plots are shown in Fig. S7b and the calculated Tafel slope values are summarized in Table S2. $MnS_{0.10}O_{1.90}/MnCo_2S_4$ possesses the lowest Tafel slope of 78 mV dec^{-1}, suggesting a more favorable reaction kinetics and rapid charge transfer rate in the OER process. It is worth noting that, $MnS_{0.10}O_{1.90}/MnCo_2S_4$ has superior OER performance to the recently reported catalyst with similar structures in alkaline solution (Table S3).

The OER performance of the $MnS_{0.10}O_{1.90}/MnCo_2S_4$ sample was then compared with the state-of-the-art IrO_2 catalyst in 1 M KOH. As shown from LSV curves in Fig. S8a and b, IrO_2 presents a high activity with an overpotential of 410 mV @ 50 mA cm^{-2}, and possesses a typical low Tafel slope value of 96 mV dec^{-1}. Nevertheless, in comparison, its activity is still inferior to that of $MnS_{0.10}O_{1.90}/MnCo_2S_4$, of which the overpotential is 367 mV @ 50 mA cm^{-2} and the Tafel slope is 78 mV dec^{-1}. To unravel the physical origin of the excellent activity of $MnS_{0.10}O_{1.90}/MnCo_2S_4$, we measured the double-layer capacitance (C_{dl}), and normalized the geometric current density to the corresponding electrochemically active surface area (ECSA) (Fig. S8c and Fig. S9). As expected, $MnS_{0.10}O_{1.90}/MnCo_2S_4$ has a larger C_{dl} of 13.31 mF cm^{-2} than IrO_2 (11.58 mF cm^{-2}), indicating that it possesses a higher ECSA value. In addition, the electrochemical impedance spectra (EIS, shown in Fig. S8d) display that the charge transfer resistance (R_{ct}) of $MnS_{0.10}O_{1.90}/MnCo_2S_4$ (4.49 Ω) is smaller than that of IrO_2 (7.62 Ω), suggesting the more effortless electron transport at the catalyst and electrolyte interface during the OER process.

Encouraged by the superior OER performance of $MnS_{0.10}O_{1.90}/MnCo_2S_4$ in alkaline media, we then investigated its OER properties in neutral electrolyte and compared with IrO_2. As shown in Fig. 3a, it requires an overpotential of 414 mV for $MnS_{0.10}O_{1.90}/MnCo_2S_4$ to reach a current density of 10 mA cm^{-2} in 0.2 M PBS solution, which is lower than that of MnO_2 (629 mV), $MnS_{0.10}O_{1.90}$ (560 mV), $MnCo_2S_4$ (480 mV), and IrO_2 (492 mV) as well, and superior to other catalysts that have been reported for OER in this condition (Table S4). The Nyquist plots (Fig. 3b) of EIS spectra reveal that the R_{ct} value of $MnS_{0.10}O_{1.90}/MnCo_2S_4$ (282 Ω) is clearly smaller than that of MnO_2 (>800 Ω), $MnS_{0.10}O_{1.90}$ (693 Ω), $MnCo_2S_4$ (310 Ω), and IrO_2 (340 Ω), indicating the more rapid charge transfer occurs during OER. Besides, the OER activity of the samples can be further attributed to the ECSA results (Fig. 3c and Fig. S10). As indicated, the ECSA value of $MnS_{0.10}O_{1.90}/MnCo_2S_4$ (1.99 mF cm^{-2}, 169.22 cm^2) is higher than that of MnO_2 (0.97 mF cm^{-2}, 82.48 cm^2), $MnS_{0.10}O_{1.90}$ (1.22 mF cm^{-2}, 103.74 cm^{-2}),
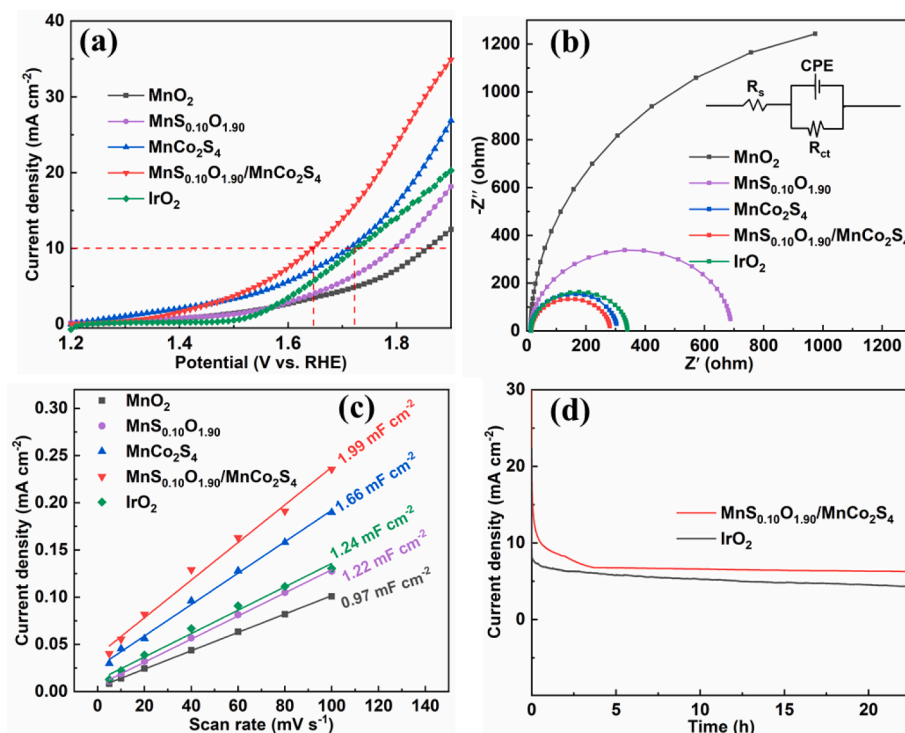
Fig. 3. (a) OER polarization curves of MnO_2, $MnS_{0.10}O_{1.90}$, $MnCo_2S_4$, $MnS_{0.10}O_{1.90}/MnCo_2S_4$, and IrO_2 in 0.2 M PBS electrolyte at a scan rate of 10 mV s^{-1}. (b) The corresponding Nyquist plots at the overpotential of 320 mV. (c) Double-layer capacitance (C_{dl}) of the synthesized samples at 1.16 V *vs.* RHE. (d) The *i-t* chronoamperometric response for $MnS_{0.10}O_{1.90}/MnCo_2S_4$ and IrO_2 at the potential of 1.6 V *vs.* RHE.

$MnCo_2S_4$ (1.66 mF cm^{-2}, 141.16 cm^2), and IrO_2 (1.24 mF cm^{-2} 105.44 cm^2). Interestingly, after the polarization curve is corrected with the ECSA value, $MnS_{0.10}O_{1.90}/MnCo_2S_4$ still exhibits an intrinsic activity comparable to that of IrO_2 (Fig. S11). It suggests that more active sites of $MnS_{0.10}O_{1.90}/MnCo_2S_4$ can be utilized in the OER process. Finally, the long-term stability of $MnS_{0.10}O_{1.90}/MnCo_2S_4$ and IrO_2 was measured by chronoamperometric test at 1.6 V *vs.* RHE in 0.2 M PBS solution. Noteworthily, the current density of $MnS_{0.10}O_{1.90}/MnCo_2S_4$ exhibits a trend of sharp decline in the initial section (Fig. 3d), presumably due to the stripping of the unstable components on the catalyst surface, while in the range from 3.5 h to 22 h, the current density of $MnS_{0.10}O_{1.90}/MnCo_2S_4$ only decreased by 5.9%, implying great robustness. As a comparison, the current density of IrO_2 attenuated from 6.12 mA cm^{-2} at 3.5 h to 4.33 mA cm^{-2} at 22 h, with a decay of 29.3%. In addition, to further compare the long-term durability of $MnS_{0.10}O_{1.90}/MnCo_2S_4$ and IrO_2, we performed the accelerate durability test. As shown in Fig. S12, the overpotential @ 10 mA cm^{-2} of $MnS_{0.10}O_{1.90}/MnCo_2S_4$ decreased by 22 mV after 5000 cycles, much smaller than that of IrO_2 (42 mV). Thus, the durability of $MnS_{0.10}O_{1.90}/MnCo_2S_4$ in neutral solution is superior than that of IrO_2 catalyst. The remarkable stability of $MnS_{0.10}O_{1.90}/MnCo_2S_4$ may be due to the facile charge transfer between the electrolyte and the catalyst, which maintains the structural integrity of the sample in long-term operation.

Subsequently, we employed theoretical calculations to unravel the reaction mechanism and identify the active center (see Supplementary Materials for simulation details). The charge density difference is shown in Fig. 4a and b, upon creating the $MnO_2/MnCo_2S_4$ heterostructure, electrons flow from $MnCo_2S_4$ to MnO_2 resulting in holes in $MnCo_2S_4$ and electrons in MnO_2. Notably, the density of state (DOS) intensity of $MnO_2/MnCo_2S_4$ is larger than that of $MnCo_2S_4$ and MnO_2 at the Fermi level, suggesting that strong interactions and effective charge transfer between $MnCo_2S_4$ and MnO_2 at the interface (Fig. 4c, Fig. S13a, b and c). The states around the interface indicate that the interface can easily undergo charge transfer with electrolyte.

Next, we performed DFT calculations to study the OER mechanism

catalyzed by $MnO_2/MnCo_2S_4$ heterostructure using a slab model. Because $MnCo_2S_4$ is at the surface of the $MnO_2/MnCo_2S_4$ heterostructure, it is easy to be oxidized during OER as evidenced by the XPS results in Fig. 2, so we first investigated the active sites using $MnCo_2O_4$ as a model catalyst. The mechanism of OER follows the Rossmeisl's work, as given in Supplementary Materials [44]. As shown in Fig. 4d and e, three active sites, Mn, Mn-Co, and Co-Co, were studied. Mn-Co has the lowest overpotential (η) of OER (0.61 V), followed by Mn (0.69 V), and Co-Co (0.75 V). The Mn site binds the oxygen-containing intermediates (OH*, O* and OOH*) too weak, because only one Mn atom can interact with the oxygen-containing intermediates in Mn site, resulting the OH*→O* step is rate-determining. Oxygen-containing intermediates can coordinate to two transition metals in Co-Co and Mn-Co sites, so these intermediates can be well stabilized. Because Co^{3+} lies in its low spin state with its anti-bonding orbitals empty, and Mn lies in high spin state and has three electrons in its anti-bonding orbitals (Fig. 4f), Co can form stronger bonds with oxygen than Mn. As a result, Co-Co site binds to oxygen containing intermediates much stronger than Mn-Co site, leading to overbinding of these intermediates to Co-Co site, resulting O*→OOH* as the rate determining step. The Mn-Co site binds to these intermediates moderately, resulting a low overpotential.

In addition, the further theoretical investigation reveals that, vunlcanization of the oxidized CoMnO active species can further promote the OER activity. As shown in Fig. 4d, Mn-Co site in CoMnO-S has a smaller η value than that in CoMnO, suggesting CoMnO-S has a higher OER activity than CoMnO, *i. e.*, CoMnS has a higher OER activity after preoxidation. The higher activity of CoMnO-S ($\eta = 0.38$ V) than CoMnO ($\eta = 0.61$ V) is attributed to its larger lattice parameter. The lattice constant of CoMnS is 5.91 Å, which is larger than that of CoMnO (5.79 Å), suggesting that the oxidized CoMnO at the surface would suffer from the tensile strain from the bulk of CoMnO-S. Because the rate-determining step of OER for Mn-Co site is O*→OOH* transformation and the bond lengths of Co-O and Mn-O for O* intermediate are smaller than that for OOH* intermediate, it can be expected that applying a tensile strain can destabilize O* intermediate more than that for OOH*
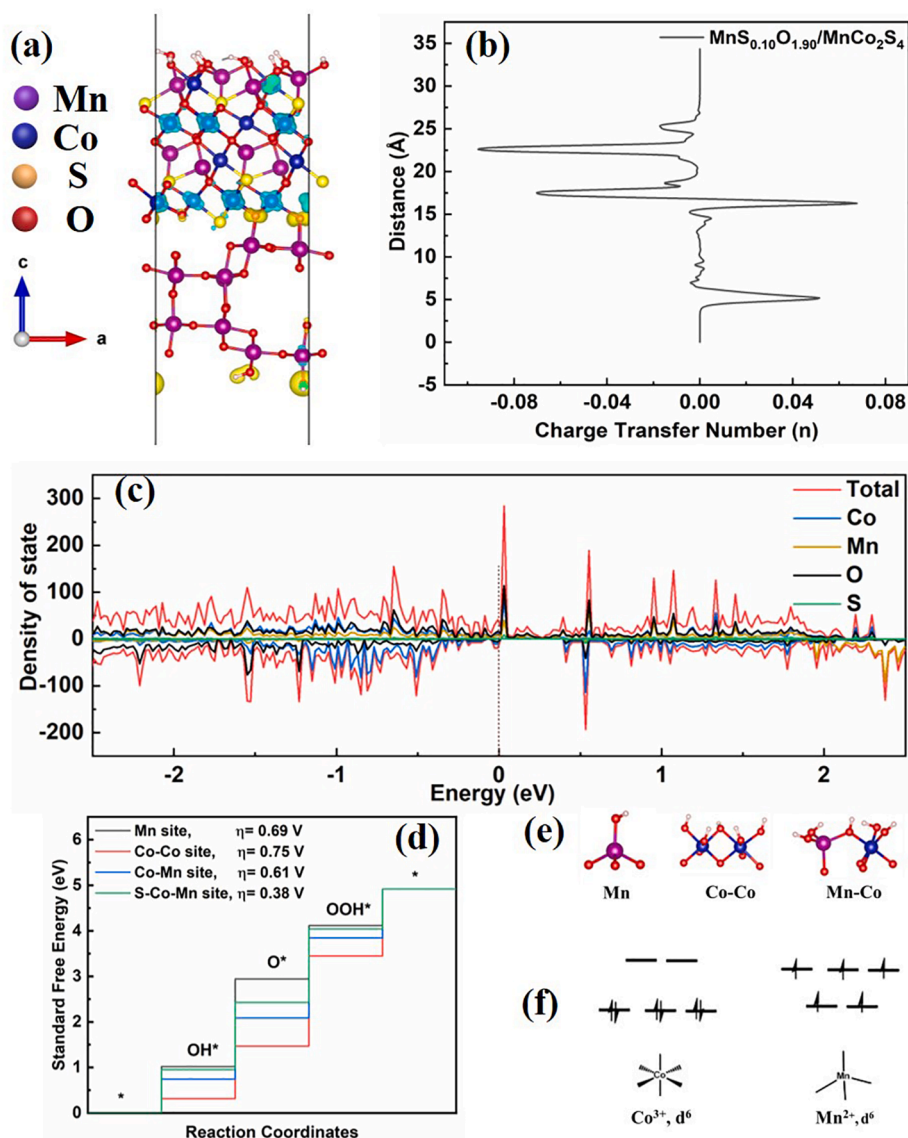
Fig. 4. (a) The charge density difference in the interface of $MnS_{0.10}O_{1.90}$-$MnCo_2S_4$. Yellow and blue areas represent electron accumulation and depletion, respectively, and the corresponding charge transfer number shown in (b). (c) Density of states (DOS) of MnO_2/$MnCo_2S_4$ systems. (d) Standard free energies of the ORR computed for different active sites of CoMnO. (e) Three different active sites of CoMnO catalyst, (f) the ligand field splitting of Co^{3+} and Mn^{2+}.

intermediate. So, the energy difference between O* and OOH* intermediate is smaller, leading to a lower η value (0.38 V) of CoMnO-S than CoMnO (0.61 V).

The $MnS_{0.10}O_{1.90}$/$MnCo_2S_4$ heterostructure with superior OER performance stimulates its application prospect in neutral ZABs. Therefore, the primary neutral ZAB was home-assembled by using $MnS_{0.10}O_{1.90}$/$MnCo_2S_4$, zinc plate, and 5 M NH_4Cl plus 0.25 M $ZnCl_2$ solution as the air cathode, anode, and electrolyte, respectively. As shown in the charge polarization curves in Fig. 5a, compared with the IrO_2-modified ZAB, the $MnS_{0.10}O_{1.90}$/$MnCo_2S_4$ based ZAB shows more superior charge performance with a larger current density. Fig. 5b illustrates that the specific capacity of the $MnS_{0.10}O_{1.90}$/$MnCo_2S_4$ modified battery is 746 mA h g^{-1} at a constant current density of 10 mA cm^{-2}, higher than the IrO_2 decorated battery (626 mA h g^{-1}). The cyclic charge–discharge stabilities were performed at the current density of 10 mA cm^{-2} with per cycle of 10 min (Fig. 5c). The $MnS_{0.10}O_{1.90}$/$MnCo_2S_4$ based ZAB exhibits superior cyclic stability for 140 h, especially during the charging process, while the IrO_2-based ZAB just sustained about 30 h. Specifically, the initial discharge and charge voltages for $MnS_{0.10}O_{1.90}$/$MnCo_2S_4$ are 2.15 V and 0.93 V, respectively, which is 0.06 V lower and 0.07 V higher

than the IrO_2-based ZAB. After continuous 140 h of operation, the voltage gap of charge–discharge for the $MnS_{0.10}O_{1.90}$/$MnCo_2S_4$-modified battery only increased from 1.22 V to 1.33 V. In stark contrast, the initial voltage gap of the IrO_2-decorated battery is 1.35 V, after cycling 34 h, the voltage gap has enlarged to 1.55 V. This performance is better than the state-of-the-art neutral ZABs (Table S5). Subsequently, we examined the microstructure of the $MnS_{0.10}O_{1.90}$/$MnCo_2S_4$ sample after the charge–discharge test by employing XRD and TEM techniques. As shown in Fig. S16a and b, the structure of $MnS_{0.10}O_{1.90}$/$MnCo_2S_4$ still retains the characteristics of the initial nanorod morphology after 140 h of cycling. Besides, Fig. S16c and d illustrate that the lattice structure has no obvious change after charge–discharge cycling. The above results prove the markedly robust stability of the $MnS_{0.10}O_{1.90}$/$MnCo_2S_4$ heterostructure, solidly corroborate that the $MnS_{0.10}O_{1.90}$/$MnCo_2S_4$ electrode possesses great potentials for practical application in neutral ZABs.

4. Conclusions

In summary, a novel $MnS_{0.10}O_{1.90}$/$MnCo_2S_4$ electrocatalyst with well-defined heterostructure is fabricated by a facile two-step

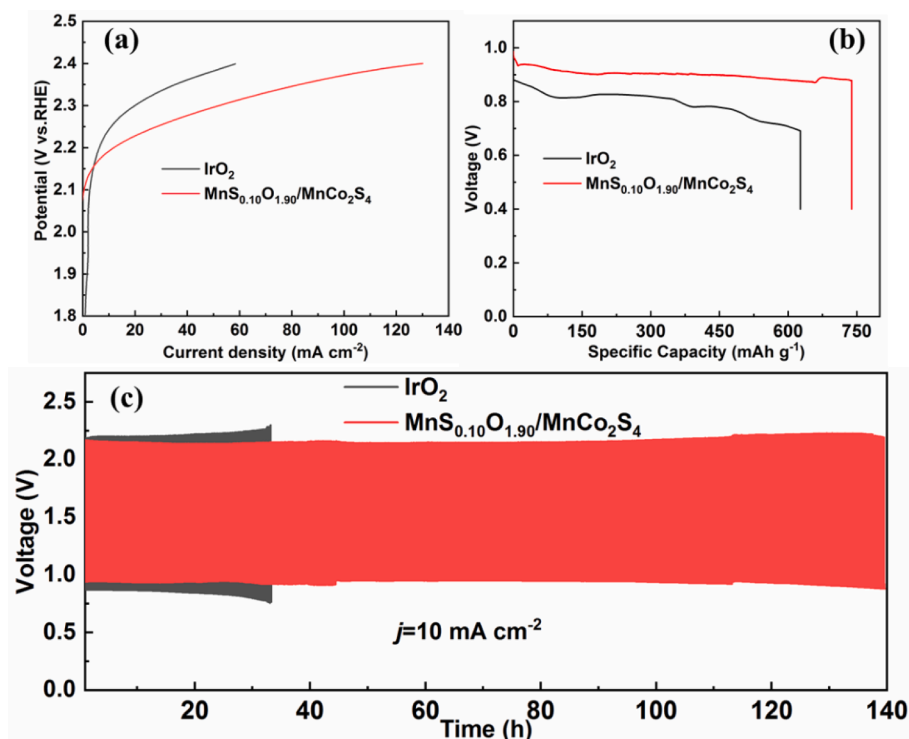**Fig. 5.** The performance of neutral Zn-air batteries based on $MnS_{0.10}O_{1.90}/MnCo_2S_4$ and IrO_2 as air cathode. (a) Charge polarization curves. (b) Specific capacities at 10 mA cm^{-2} and (c) Galvanostatic charge − discharge test at 10 mA cm^{-2} in neutral electrolyte.

hydrothermal method. The morphological structure, crystal lattice, chemical constituent, and electronic state of the $MnS_xO_{2-x}/MnCo_2S_4$ heterostructure can be modulated by optimizing the stoichiometric ratio of sulfur-to-oxygen. The sample of $MnS_{0.10}O_{1.90}/MnCo_2S_4$ displays the most outstanding OER performance in both half-cell and primary ZABs. Particularly, in neutral operating conditions, $MnS_{0.10}O_{1.90}/MnCo_2S_4$ presents lower overpotential (414 mV @ 10 mA cm^{-2}), charge transfer resistance (282 Ω), and higher ECSA (1.99 mF cm^{-2}) value than IrO_2 (492 mV, 340 Ω, and 1.24 mF cm^{-2}, respectively) for OER. Most importantly, $MnS_{0.10}O_{1.90}/MnCo_2S_4$ as the OER catalyst for neutral ZAB shows a low charging voltage of 2.15 V and maintains superior robust cycling stability. Such intriguing performance is mainly attributed to its unique interfacial heterostructure. DFT calculations revealed that the Mn-Co site has the suitable binding affinity to the oxygen-containing intermediates rather than Co-Co or Mn-sites. $MnCo_2S_4$ can induce tensile strain to the oxidized CoMnO to destabilize the O* intermediate resulting a lower energy difference between O* and OOH* to lower the overpotential. This work provides a new strategy to boost the OER performance by engineering the electronic structure and strain of the heterostructure interfaces, and it opens a new avenue for developing high-performance and durable heterostructure electrocatalysts toward OER, metal-air batteries in neural electrolytes and beyond.

Declaration of Competing Interest

The authors declare that they have no known competing financial interests or personal relationships that could have appeared to influence the work reported in this paper.

Acknowledgements

Appendix A. Supplementary data

Supplementary data to this article can be found online at https://doi.org/10.1016/j.cej.2021.131966.

References

[1] T. Wu, S. Sun, J. Song, S. Xi, Y. Du, B. Chen, W.A. Sasangka, H. Liao, C.L. Gan, G. G. Scherer, L. Zeng, H. Wang, H. Li, A. Grimaud, Z.J. Xu, Iron-facilitated dynamic active-site generation on spinel CoAl2O4 with self-termination of surface reconstruction for water oxidation, Nat. Catal. 2 (2019) 763–772.

[2] J. Zhang, Q. Zhang, X. Feng, Support and interface effects in water-splitting electrocatalysts, Adv. Mater. 31 (2019) 1808167.

[3] H.-J. Qiu, P. Du, K. Hu, J. Gao, H. Li, P. Liu, T. Ina, K. Ohara, Y. Ito, M. Chen, Metal and nonmetal codoped 3D nanoporous graphene for efficient bifunctional electrocatalysis and rechargeable Zn–Air batteries, Adv. Mater. 31 (2019) 1900843.

[4] A. Pirkarami, S. Rasouli, E. Ghasemi, 3-D CdS@NiCo layered double hydroxide core-shell photoelectrocatalyst used for efficient overall water splitting, Appl. Catal. B-Environ. 241 (2019) 28–40.

[5] Y. Li, J. Fu, C. Zhong, T. Wu, Z. Chen, W. Hu, K. Amine, J. Lu, Recent advances in flexible zinc-based rechargeable batteries, Adv. Energy. Mater. 9 (2019) 1802605.

[6] H.-F. Wang, C. Tang, Q. Zhang, A review of precious-metal-free bifunctional oxygen electrocatalysts: rational design and applications in Zn−Air batteries, Adv. Funct. Mater. 28 (2018) 1803329.

[7] H. Li, L. Ma, C. Han, Z. Wang, Z. Liu, Z. Tang, C. Zhi, Advanced rechargeable zinc-based batteries: recent progress and future perspectives, Nano Energy 62 (2019) 550–587.

[8] L. Ma, S. Chen, D. Wang, Q. Yang, F. Mo, G. Liang, N. Li, H. Zhang, J.A. Zapien, C. Zhi, Super-stretchable zinc-air batteries based on an alkaline-tolerant dual-network hydrogel electrolyte, Adv. Energy Mater. 9 (2019) 1803046.

[9] A.R. Mainar, E. Iruin, L.C. Colmenares, A. Kvasha, I. de Meatza, M. Bengoechea, O. Leonet, I. Boyano, Z. Zhang, J.A. Blazquez, An overview of progress in electrolytes for secondary zinc-air batteries and other storage systems based on zinc, J. Energy Storage 15 (2018) 304–328.

[10] S. Clark, A.R. Mainar, E. Iruin, L.C. Colmenares, J.A. Blázquez, J.R. Tolchard, A. Latz, B. Horstmann, Towards rechargeable zinc–air batteries with aqueous chloride electrolytes, J. Mater. Chem. A 7 (2019) 11387–11399.

[11] A. Sumboja, X. Ge, G. Zheng, F.W.T. Goh, T.S.A. Hor, Y. Zong, Z. Liu, Durable rechargeable zinc-air batteries with neutral electrolyte and manganese oxide catalyst, J. Power Sour. 332 (2016) 330–336.

[12] L. An, Z. Zhang, J. Feng, F. Lv, Y. Li, R. Wang, M. Lu, R.B. Gupta, P. Xi, S. Zhang, Heterostructure-promoted oxygen electrocatalysis enables rechargeable zinc-air battery with neutral aqueous electrolyte, J. Am. Chem. Soc. 140 (2018) 17624–17631.

[13] F.W. Goh, Z. Liu, T. Hor, J. Zhang, X. Ge, Y. Zong, A. Yu, W. Khoo, A near-neutral chloride electrolyte for electrically rechargeable zinc-air batteries, J. Electrochem. Soc. 161 (2014) A2068–A2079.

[14] S. Clark, A. Latz, B. Horstmann, Rational development of neutral aqueous electrolytes for Zinc-air batteries, ChemSusChem 10 (2017) 4735–4747.

[15] L.C. Seitz, C.F. Dickens, K. Nishio, Y. Hikita, J. Montoya, A. Doyle, C. Kirk, A. Vojvodic, H.Y. Hwang, J.K. Norskov, T.F. Jaramillo, A highly active and stable IrOx/SrIrO3 catalyst for the oxygen evolution reaction, Science 353 (2016) 1011.

[16] Y. Lee, J. Suntivich, K.J. May, E.E. Perry, Y. Shao-Horn, Synthesis and activities of rutile IrO2 and RuO2 nanoparticles for oxygen evolution in acid and alkaline solutions, J. Phys. Chem. Lett. 3 (2012) 399–404.

[17] Q. Qian, Y. Li, Y. Liu, L. Yu, G. Zhang, Ambient fast synthesis and active sites deciphering of hierarchical foam-like trimetal-organic framework nanostructures as a platform for highly efficient oxygen evolution electrocatalysis, Adv. Mater. 31 (2019) 1901139.

[18] B.S. Yeo, A.T. Bell, Enhanced activity of gold-supported cobalt oxide for the electrochemical evolution of oxygen, J. Am. Chem. Soc. 133 (2011) 5587–5593.

[19] R. Subbaraman, D. Tripkovic, K.-C. Chang, D. Strmcnik, A.P. Paulikas, P. Hirunsit, M. Chan, J. Greeley, V. Stamenkovic, N.M. Markovic, Trends in activity for the water electrolyser reactions on 3d M(Ni Co, Fe, Mn) hydr(oxy)oxide catalysts, Nat. Mater. 11 (2012) 550–557.

[20] C.C.L. McCrory, S. Jung, J.C. Peters, T.F. Jaramillo, Benchmarking heterogeneous electrocatalysts for the oxygen evolution reaction, J. Am. Chem. Soc. 135 (2013) 16977–16987.

[21] Y. Sun, H. Liao, J. Wang, B. Chen, S. Sun, S.J.H. Ong, S. Xi, C. Diao, Y. Du, J.-O. Wang, M.B.H. Breese, S. Li, H. Zhang, Z.J. Xu, Covalency competition dominates the water oxidation structure–activity relationship on spinel oxides, Nat. Catal. 3 (2020) 554–563.

[22] F. Song, X. Hu, Exfoliation of layered double hydroxides for enhanced oxygen evolution catalysis, Nat. Commun. 5 (2014) 4477.

[23] S. Chen, J. Duan, P. Bian, Y. Tang, R. Zheng, S.-Z. Qiao, Three-dimensional smart catalyst electrode for oxygen evolution reaction, Adv. Energy Mater. 5 (2015) 1500936.

[24] X. Ren, C. Wei, Y. Sun, X. Liu, F. Meng, X. Meng, S. Sun, S. Xi, Y. Du, Z. Bi, G. Shang, A.C. Fisher, L. Gu, Z.J. Xu, Constructing an adaptive heterojunction as a highly active catalyst for the oxygen evolution reaction, Adv. Mater. 32 (2020) 2001292.

[25] Y. Zhang, J. Fu, H. Zhao, R. Jiang, F. Tian, R. Zhang, Tremella-like Ni3S2/MnS with ultrathin nanosheets and abundant oxygen vacancies directly used for high speed overall water splitting, Appl. Catal. B-Environ. 257 (2019), 117899.

[26] Y. Wang, J. Fu, Y. Zhang, M. Li, F.M. Hassan, G. Li, Z. Chen, Continuous fabrication of a MnS/Co nanofibrous air electrode for wide integration of rechargeable zinc–air batteries, Nanoscale 9 (2017) 15865–15872.

[27] J.-Y. Wang, W.-T. Liu, X.-P. Li, T. Ouyang, Z.-Q. Liu, Strong hydrophilicity NiS2/Fe7S8 heterojunctions encapsulated in N-doped carbon nanotubes for enhanced oxygen evolution reaction, Chem. Commun. 56 (2020) 1489–1492.

[28] W.-K. Han, X.-P. Li, L.-N. Lu, T. Ouyang, K. Xiao, Z.-Q. Liu, Partial S substitution activates NiMoO4 for efficient and stable electrocatalytic urea oxidation, Chem. Commun. 56 (2020) 11038–11041.

[29] Y. Sun, S. Sun, H. Yang, S. Xi, J. Gracia, Z.J. Xu, Spin-related electron transfer and orbital interactions in oxygen electrocatalysis, Adv. Mater. 32 (2020) 2003297.

[30] L. An, J. Feng, Y. Zhang, R. Wang, H. Liu, G.-C. Wang, F. Cheng, P. Xi, Epitaxial heterogeneous interfaces on N-NiMoO4/NiS2 nanowires/nanosheets to boost hydrogen and oxygen production for overall water splitting, Adv. Funct. Mater. 29 (2019) 1805298.

[31] W. Jin, J. Chen, B. Liu, J. Hu, Z. Wu, W. Cai, G. Fu, Oxygen vacancy-rich in-doped CoO/CoP heterostructure as an effective air cathode for rechargeable Zn–air batteries, Small 15 (2019) 1904210.

[32] J. Zhang, T. Wang, D. Pohl, B. Rellinghaus, R. Dong, S. Liu, X. Zhuang, X. Feng, Interface engineering of MoS2/Ni3S2 heterostructures for highly enhanced electrochemical overall-water-splitting activity, Angew. Chem. Int. Ed. 55 (2016) 6702–6707.

[33] X. Luo, P. Ji, P. Wang, R. Cheng, D. Chen, C. Lin, J. Zhang, J. He, Z. Shi, N. Li, S. Xiao, S. Mu, Interface engineering of hierarchical branched Mo-Doped Ni3S2/NixPy hollow heterostructure nanorods for efficient overall water splitting, Adv. Energy Mater. 10 (2020) 1903891.

[34] Q. Liu, J. Huang, Y. Zhao, L. Cao, K. Li, N. Zhang, D. Yang, L. Feng, L. Feng, Tuning the coupling interface of ultrathin Ni3S2@NiV-LDH heterogeneous nanosheet electrocatalysts for improved overall water splitting, Nanoscale 11 (2019) 8855–8863.

[35] J. Yin, J. Jin, M. Lu, B. Huang, H. Zhang, Y. Peng, P. Xi, C.-H. Yan, Iridium single atoms coupling with oxygen vacancies boosts oxygen evolution reaction in acid media, J. Am. Chem. Soc. 142 (2020) 18378–18386.

[36] X. Wang, Y. Li, Synthesis and formation mechanism of manganese dioxide nanowires/nanorods, Chem. – Eur. J. 9 (2003) 300–306.

[37] Y. Dong, J. Zhao, J.-Y. Zhang, Y. Chen, X. Yang, W. Song, L. Wei, W. Li, Synergy of Mn and Ni enhanced catalytic performance over toluene combustion over Ni-doped α-MnO2 catalysts, Chem. Eng. J. 388 (2020), 124244.

[38] A. Khan, H. Wang, Y. Liu, A. Jawad, J. Ifthikar, Z. Liao, T. Wang, Z. Chen, Highly efficient α-Mn2O3@α-MnO2-500 nanocomposite for peroxymonosulfate activation: comprehensive investigation of manganese oxides, J. Mater. Chem. A 6 (2018) 1590–1600.

[39] J. Lin, P. Wang, H. Wang, C. Li, X. Si, J. Qi, J. Cao, Z. Zhong, W. Fei, J. Feng, Defect-rich heterogeneous MoS2/NiS2 nanosheets electrocatalysts for efficient overall water splitting, Adv. Sci. 6 (2019) 1900246.

[40] L. Abbasi, M. Arvand, S.E. Moosavifard, Facile template-free synthesis of 3D hierarchical ravine-like interconnected MnCo2S4 nanosheet arrays for hybrid energy storage device, Carbon 161 (2020) 299–308.

[41] X. Zhang, X. Li, R. Li, Y. Lu, S. Song, Y. Wang, Highly active core-shell carbon/NiCo2O4 double microtubes for efficient oxygen evolution reaction: ultralow overpotential and superior cycling stability, Small 15 (2019) 1903297.

[42] H. Zhang, X. Li, A. Hähnel, V. Naumann, C. Lin, S. Azimi, S.L. Schweizer, A.W. Maijenburg, R.B. Wehrspohn, Bifunctional heterostructure assembly of NiFe LDH nanosheets on NiCoP nanowires for highly efficient and stable overall water splitting, Adv. Funct. Mater. 28 (2018) 1706847.

[43] G. Liu, B. Wang, T. Liu, L. Wang, H. Luo, T. Gao, F. Wang, A. Liu, D. Wang, 3D self-supported hierarchical core/shell structured MnCo2O4@CoS arrays for high-energy supercapacitors, J. Mater. Chem. A 6 (2018) 1822–1831.

[44] J. Rossmeisl, A. Logadottir, J.K. Nørskov, Electrolysis of water on (oxidized) metal surfaces, Chem. Phys. 319 (2005) 178–184.